

Streamlines of the Mean Stellar Motions in Elliptical Galaxies

R. F. Anderson^{1,3} and Thomas S. Statler^{1,2,4}

ABSTRACT

The stellar velocity fields of elliptical galaxies hold clues to their dynamical structure and origin. The construction of velocity field models is greatly simplified by assuming an approximate geometrical form for the streamlines of the mean stellar motions, for example, representing the streamlines of short-axis and long-axis tube orbits by coordinate lines in a confocal coordinate system. A single confocal system precisely fits the mean motions of all tube orbits in a Stäckel potential; but these potentials are not sufficiently general. Here we test the conjecture that confocal streamlines may still be a valid approximation for more realistic triaxial systems. We numerically integrate orbits in Schwarzschild's (1993) logarithmic potential. Six sets of axis ratios are used; in each, ~ 50 orbits, comprising short-axis and long-axis tubes as well as some resonant families, are integrated for ~ 20000 dynamical times and the average velocity is found in each of ~ 4000 spatial cells. Confocal streamlines are compared to the velocity field by finding the RMS magnitude of the cross product between the velocity vectors and the streamlines. Minimizing this quantity yields a best fit confocal system for each orbit. We find that the great majority of orbits at a given energy in each potential can be fitted by nearly identical confocal systems. There are statistically significant differences between the average streamline parameters obtained for different orbit families, but the differences are small. We show that the fitted parameters reproduce, to high accuracy, the location of the boundary between short axis and outer long axis tubes, which is a direct measure of the triaxiality of the potential. These results strongly support efforts to obtain accurate statistical measurements of triaxiality from kinematic observations and reasonably simple velocity field models.

Subject headings: galaxies: elliptical and lenticular, cD — galaxies: kinematics and dynamics

¹Department of Physics and Astronomy, University of North Carolina, Chapel Hill, NC 27559-3255

²Present address: Department of Physics and Astronomy, Ohio University, Athens, OH 45701

³boband@physics.unc.edu

⁴tss@coma.phy.ohiou.edu

1. Introduction

The stellar velocity fields of elliptical galaxies are important diagnostics of their intrinsic shapes and dynamical structure, which in turn hold clues to their origin and evolution. Methods to extract structural information from the observable velocity fields, initially developed by Binney (1985), have been greatly expanded upon by Franx, Illingworth and de Zeeuw (1991), Tenjes *et al.* (1992, 1993), and Statler (1994a,b), among others. The construction of velocity field models is a complex task, particularly if the dynamical model is required to be fully self-consistent; some velocity field models of this sort have been laboriously calculated (*e.g.*, Statler 1991, Arnold *et al.* 1994). The methods cited above, however, sidestep the computational bottleneck of self-consistency by adopting geometrical approximations for the streamlines of the mean stellar motions and then solving the equation of continuity.

In most of these models, the mean stellar flow is assumed to follow elliptical streamlines in parallel planes. In Binney’s (1985) models, the streamlines are tangent to the equidensity surfaces and perpendicular to the long or short axes of the figure. The models of Tenjes *et al.* (1992) are similar but allow an arbitrary tilt with respect to the principal axes. Franx *et al.* (1991) use circular or elliptical streamlines aligned either with or contrary to the equidensity surfaces and perpendicular to the short axis. (Cf. Figure 1 of Statler 1996.)

A somewhat different approach is taken by Statler (1994a), who calculates mean stellar motions as vector sums of two intersecting collisionless flows created by short-axis and long-axis tube orbits. The streamlines for these flows are assumed to follow coordinate lines in a confocal ellipsoidal coordinate system. In the special class of Stäckel potentials, a single such confocal system gives a set of streamlines that precisely fit the mean motions of all orbits in a given potential; consequently the same system fits the total short-axis and long-axis mean flows, regardless of the form of the distribution function. Unfortunately, the Stäckel potentials are not sufficiently general to be realistic models for elliptical galaxies (Binney 1987, Merritt & Fridman 1996). In non-Stäckel potentials, one should not expect a set of confocal streamlines to precisely fit the mean motion of an arbitrary orbit, or that streamlines fitted to different orbits will come from the same confocal system. Nonetheless, it is possible that confocal streamlines may be a valid approximation for the combined mean motions of many orbits in realistic triaxial systems.

In this paper we test this conjecture, by fitting confocal streamlines to the mean velocities of individual numerically integrated tube orbits in a set of realistic non-rotating scale-free potentials (Schwarzschild 1993). For each orbit, mean velocity vectors are computed over a fine spatial grid; we then find the parameters of the confocal system for which the relevant coordinate lines are most nearly tangent to the mean velocities. For all axis ratios tested, the parameters of the fitted confocal system are weak functions of the integrals of motion. Thus, at a given energy in a given potential, a single confocal system provides an excellent fit to the mean motions of short-axis tubes, long-axis tubes, and the dominant higher-order resonances. Scaling to other energies is straightforward since the potentials are scale-free. We conclude that the assumption of confocal streamlines can be used

to create realistic velocity field models for elliptical galaxies that do not have significant figure rotation.

The remainder of this paper is arranged as follows. In section 2 we remind the reader of the properties of the Schwarzschild (1993) logarithmic potential and describe our methods for numerical integration of the orbits and fitting of streamlines. In section 3 we present our results and in section 4 discuss their implications.

2. Approach

2.1. Model Potentials

We adopt for this study Schwarzschild’s (1993; hereafter S93) version of the scale-free logarithmic potential, given by

$$V = \frac{1}{2} \left(\ln r^2 + c_1 \frac{z^2}{r^2} + c_2 \frac{y^2}{r^2} + c_3 \frac{z^4}{r^4} + c_4 \frac{z^2 y^2}{r^4} + c_5 \frac{y^4}{r^4} + c_6 \frac{z^6}{r^6} + c_7 \frac{z^4 y^2}{r^6} + c_8 \frac{z^2 y^4}{r^6} + c_9 \frac{y^6}{r^6} \right). \quad (1)$$

The constants c_1 through c_9 depend on the axis ratios of the mass density distribution, which is close to, though not exactly, ellipsoidal. These constants are tabulated by Schwarzschild for six sets of axis ratios, which we also adopt here. In columns 2 and 3 of Table 1 we list for each figure the triaxiality $T_m = (1 - b_m^2)/(1 - c_m^2)$ and the short-to-long axis ratio c_m of the mass distribution (where, in the definition of T_m , b_m is the middle-to-long axis ratio.) We can obtain analogous quantities for the potential, despite the slightly non-ellipsoidal shape of the equipotential surfaces, from the points at which these surfaces cross the principal axes. If these crossings occur at locations x_c , y_c , and z_c along the x , y and z axes, then

$$\ln x_c^2 = \ln y_c^2 + c_2 + c_5 + c_9 = \ln z_c^2 + c_1 + c_3 + c_6. \quad (2)$$

We thus obtain

$$b_p = \frac{y_c}{x_c} = e^{-\frac{c_2+c_5+c_9}{2}}, \quad c_p = \frac{z_c}{x_c} = e^{-\frac{c_1+c_3+c_6}{2}}. \quad (3)$$

The triaxiality T_p and axis ratio c_p of the potential are given in columns 4 and 5 of Table 1.

In this paper we eschew the simpler version of the logarithmic potential, $V = 1/2 \ln(x^2 + y^2/b^2 + z^2/c^2)$. This version is less astrophysically realistic than equation (1) because it derives from a density that becomes dimpled on the z axis as the flattening increases and turns negative at $c < 0.707$ (Binney & Tremaine 1987). We have, however, repeated our calculations for the analogue of Model 2, and obtain results qualitatively the same as those described below.

The logarithmic potential (1) is unlike most triaxial Stäckel potentials in two important ways. First, the potential can remain significantly nonspherical to large radii; second, both the potential

and the density are singular at $r = 0$. The inner r^{-2} density profile implied by the logarithmic potential is consistent with the steeper surface brightness cusps observed by the HST WF/PC (Lauer *et al.* 1995). The triaxial logarithmic potential is the best studied case in which a central mass concentration causes the majority of regular box orbits to be replaced by isolated resonant islands in a stochastic sea (Miralda-Escudé & Schwarzschild 1989, Lees & Schwarzschild 1992); it is conjectured (Merritt & Fridman 1996, Merritt & Valluri 1996) that this loss of box orbits may render triaxial equilibria impossible for the observed steep-cusped systems, or at least cause them to evolve on a time scale comparable to or less than a Hubble time. We take the view that determining whether or not steep-cusped ellipticals actually are triaxial, and consequently whether or not such a mechanism is at work, is fundamentally an observational problem. Our broad goal here is to have the ability to construct triaxial models that are in principle falsifiable by kinematic observations.

2.2. Numerical Integration of Orbits

Since the potential is scale-free, the orbital structure is the same at all energies. Following standard practice, we calculate orbits at $E = 0$. This choice plus the overall constant of proportionality in equation (1) set the units of length and time. The zero-energy x -axial orbit (which is unstable for all cases studied here) has unit amplitude and period $T_x = 2(2\pi)^{1/2} \approx 5$ for all axis ratios; the circular orbit in the spherical potential lies at $r_c = e^{-1/2} \approx 0.6$ and has period $T_c = 2\pi e^{-1/2} \approx 3.8$.

A test particle launched from a given point in the x - z plane has a velocity whose magnitude is fixed by the potential at that point and the total energy (here zero). If the direction is taken to be perpendicular to the x - z plane, then its orbit is determined uniquely by the initial point (x_0, z_0) . This defines the “ x - z start space”, in which S93 maps the boundaries of the major orbit families. The x - z start space is not complete, since not all orbits cross the x - z plane with $v_x = v_z = 0$. It does, however, include all of the short-axis (S) tubes and the inner (I) and outer (O) long-axis tubes, which are responsible for the mean rotation in models with stationary figures. Since the I tubes are low angular momentum orbits, they generally contribute far less to the observable signature than the other families except possibly in very prolate figures. We pick, for each figure, ~ 50 orbits from the O and S tube regions. We include a few I tubes in the models in which they are potentially important. In models 3 and 4 we also include the resonant “saucer” (s) orbits which replace S tubes in a significant part of the start space. For brevity we refer to the orbits by model number and start space coordinates; *e.g.*, (2, .63, .12) is the orbit launched from $(x_0, z_0) = (.63, .12)$ in Model 2.

Orbits are integrated using a fourth order Runge-Kutta method with a variable time step. The step size is set equal to $0.01r$, where r is the distance of the particle from the origin at the start of the step. Energy conservation is always better than 10^{-6} (where typical kinetic energies are of order 10^{-1}) over integrations of several tens of thousands of dynamical times. Each orbit is first integrated to $t = 5000$ to determine its family and maximum extent in the x , y , and z directions.

The volume bounded by the planes $x = \pm|x_{\max}|$, $y = \pm|y_{\max}|$, $z = \pm|z_{\max}|$ is then divided into cells, with 20 cell widths in each dimension. Owing to the symmetry of the potential, each (x_0, z_0) in the first quadrant represents four orbits related by reflection. We enforce symmetry of the grid across the principal planes to simplify averaging the computed orbit with its reflections. The number of cells N_c actually visited by the orbit is typically ~ 4000 , but depends on eccentricity and varies from ~ 1000 to ~ 6000 . Because we average reflections of each orbit the number of *independent* grid points is one fourth as large. Once the grid is defined, an integration to $t = 80000$ is performed and the time-average velocity vector calculated for each cell i . Note that the mean velocity is not equal, either in magnitude or direction, to the instantaneous speed of the particle on any passage through the cell, except in the case of periodic orbits. These vectors are then normalized to produce a field of velocity unit vectors \hat{v}_i in three dimensional space.

2.3. Fitting of Streamlines

In the confocal ellipsoidal coordinate system (λ, μ, ν) ,⁵ streamlines for S tubes and saucer orbits should lie close to lines $\mu = \text{constant}$, and those for O and I tubes close to lines $\nu = \text{constant}$. The shapes of the coordinate lines depend on two parameters, (T, Δ) , which determine the locations of the foci. In terms of the conventional notation, $T = (\beta - \alpha)/(\gamma - \alpha)$ and $\Delta = (\gamma - \alpha)^{1/2}$. The points $z = \pm\Delta$ mark the foci, and the polar angle $\theta_f = \sin^{-1} T^{1/2}$ the asymptote, of the focal hyperbola, which in Stäckel potentials is the boundary between O and S tubes in the x - z start space. In the limit $\Delta \rightarrow 0$, the focal hyperbola collapses onto the asymptote, the coordinate system becomes scale free, and motion along $\mu = \text{constant}$ or $\nu = \text{constant}$ streamlines is over spherical shells (see Figures 2, 11, and 12 of Statler 1994a.) For finite Δ the mean motion is over ellipsoidal shells that become progressively rounder at larger radius.

For each orbit we obtain, at the center of each cell i , the unit vector $\hat{\tau}_i$ in the μ or ν direction (depending on the family classification done previously) and resolve it into cartesian components. We then form the goodness of fit parameter

$$Q^2 = \frac{1}{N_c} \sum_{i=1}^{N_c} |\hat{\tau}_i \times \hat{v}_i|^2, \quad (4)$$

and minimize with respect to (T, Δ) . The two-dimensional minimization is straightforward and can be done by standard numerical methods.

⁵We use the notation for confocal coordinates defined by Lynden-Bell (1962) and reintroduced by de Zeeuw (1985). Coordinate transformations and other basic formulae can be found in either of those references.

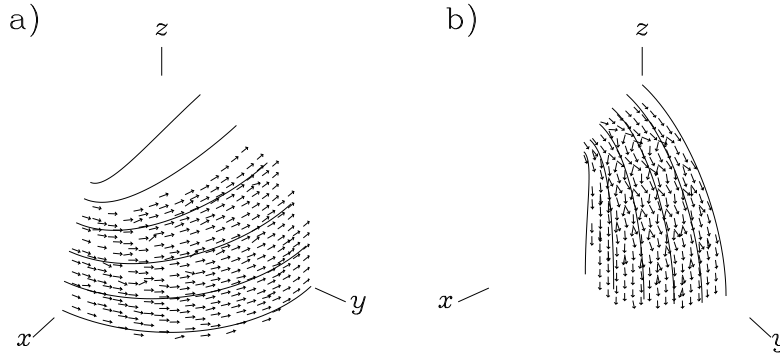


Fig. 1.— Examples of confocal streamline fits to the mean motions in two thin tube orbits: (a) the S tube launched from $(x_0, z_0) = (.48, .35)$ in Model 1; (b) the O tube launched from $(x_0, z_0) = (.23, .44)$ in Model 3. Arrows show the numerically computed normalized velocity field \hat{v} , solid curves representative streamlines in best fit confocal system. The S tube illustrates a very good fit, the O tube a fair fit typical of orbits close to family boundaries.

3. Results

Two examples of streamline fits are shown in figure 1. We specifically show thin tube orbits here for clarity, so that streamlines on one shell suffice. The S tube $(1, .48, .35)$ is fitted by the $\mu = \text{constant}$ lines on the shell $\lambda + \alpha = 0.309$ in a coordinate system with $T = 0.481$, $\Delta = 0.263$. The O tube $(3, .23, .44)$ is fitted by $\nu = \text{constant}$ lines on the $\lambda + \alpha = 0.101$ shell in the system with $T = 0.551$, $\Delta = 0.214$. The quality of the S tube fit is very good ($Q = 0.096$), whereas the O tube fit is formally a bit worse ($Q = 0.245$) owing to effects we discuss in section 3.4 below.

Figure 1 demonstrates that the velocity fields of individual orbits can be fitted by streamlines built from a confocal coordinate system. But the more central issue is whether the *same* coordinate system can adequately fit a wide variety of orbits in the same potential.

3.1. Triaxiality Measured by Streamlines

Our main result is presented in Figure 2. Each panel in the figure shows the x - z start space for one of the models. The solid curve marks the zero-velocity surface. The inner, roughly quarter-circular, dotted line marks the locus of infinitesimally thin S and O tubes. Launching points interior to this locus produce copies of orbits launched exterior to it; thus all circulating orbits lie in the annulus between the zero-velocity surface and the thin-tube boundary. Other dotted lines in the figure mark the approximate boundaries between the major orbit families, though their exact locations are problematical because of the abundance of high-order resonant islands and stochastic layers near these boundary regions. (Ignore, for the moment, the long-dashed hyperbola, which we discuss in section 3.4.) The O and S tubes are the major areas marked off in the upper left and

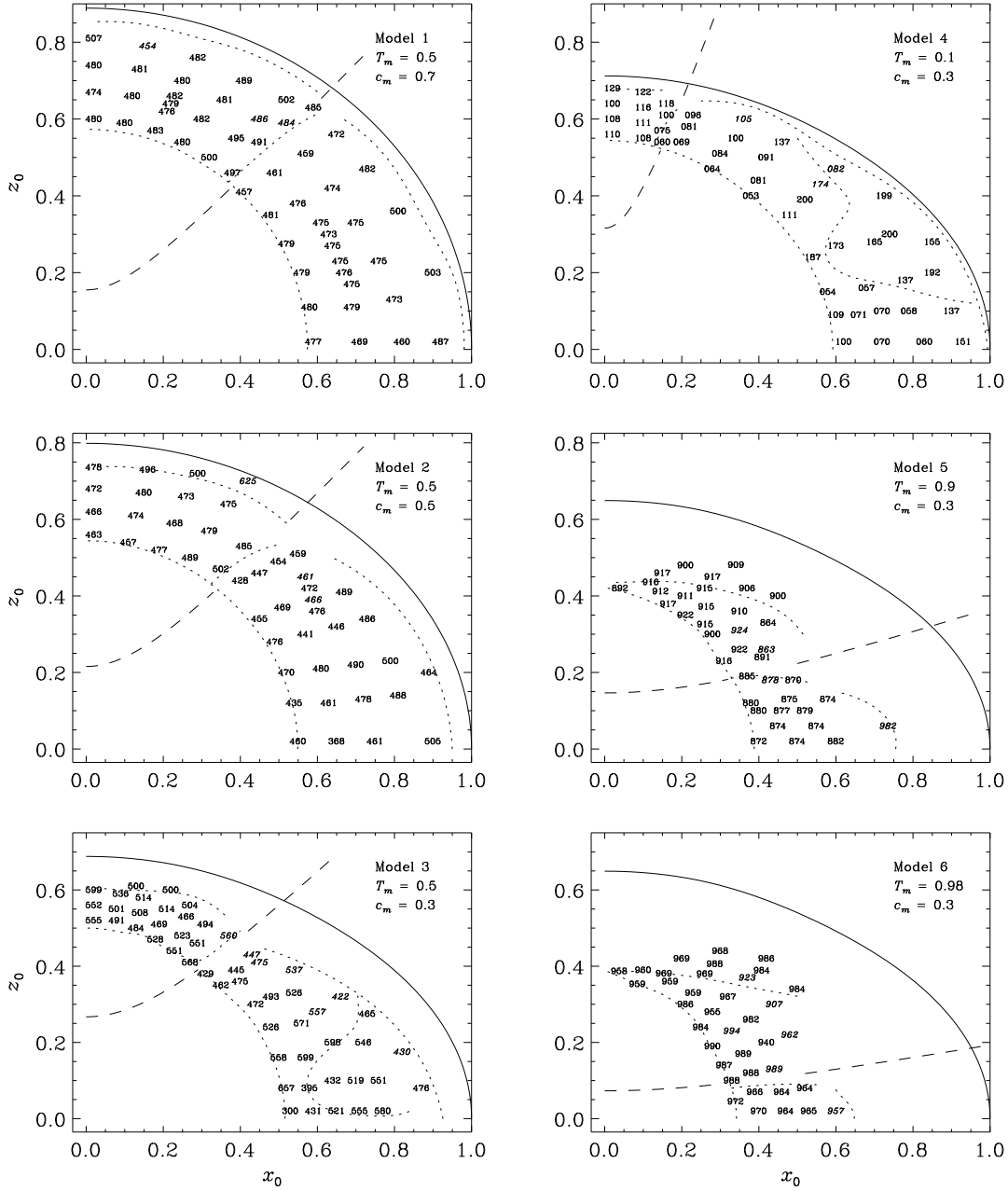


Fig. 2.— Best-fit streamline triaxiality parameters T are shown in the x - z start space for each model (leading decimal points omitted for clarity). In each panel, circulating orbits lie between the zero-velocity surface (*solid line*) and the locus of infinitesimally thin O and S tubes (*roughly concentric dotted line*). Other *dotted lines* mark the boundaries between orbit families. O and S tubes occupy the major regions in the upper left and lower right, respectively. I tubes lie above the O tubes, and saucers occupy a region within the S tubes in Models 3 and 4. The small variation in T values for each model indicates the success of the confocal streamline assumption for most orbits (section 3.1). *Italics* indicate orbits identified with specific resonances (section 3.4). The focal hyperbola defined by the average T and Δ for each model (*dashed line*) reproduces the actual O/S boundary with excellent accuracy (section 3.3).

lower right, respectively. Box orbits lie outside the S tubes. I tubes lie above the O tubes, but do not extend all the way to the zero-velocity surface because the thin I tube locus intervenes. In the panels for Models 3 and 4 we also show the saucer orbit region within the S tubes. The reader is referred to S93 for further details of the phase space structure.

At the location of each computed regular orbit we indicate the fitted value of the streamline triaxiality parameter T (omitting the leading decimal point for clarity). Three things are evident from the figure: First, the variation of T over each start space is small; in no case is the standard deviation greater than 0.06. Second, there is little indication of systematic trends across the start spaces, except at the major family boundaries in some of the models. Finally, the fitted T values are quite close to the true triaxialities T_m .

These results are quantified in columns 2 and 3 of Table 2, where we give means and standard deviations of T obtained for the major orbit families separately and for all orbits taken together. (These are unweighted means; we make no attempt to compute exact phase space volumes for the orbits or to correct for our non-uniform sampling of the start spaces.) There are differences in $\langle T \rangle$ that are significant at the 3σ or greater level between the O and S tubes in Models 1 and 5, and between the S tubes and saucers in Model 4. The O and S tubes differ by $\sim 2\sigma$ in Models 2 and 4, and by slightly over 1σ in Models 3 and 6. The T values of the O and I tubes are indistinguishable.

The average $\langle T \rangle$ over all orbits is repeated for each model in the last column of Table 1. There is excellent agreement between the triaxialities obtained from the streamline fits and the actual density and potential triaxialities of the models. In fact, there is a weak tendency for the streamline fits to reproduce T_p more accurately than T_m , though the set of mass models tested is too small to establish this firmly. It may be merely fortuitous, that the non-monotonic variation of T_p with c_m at fixed $T_m = 0.5$ is reproduced qualitatively by the streamline fits.

3.2. Radial Mean Motions

Radial mean motions are associated with asphericity of the fiducial shells on which the streamlines lie, and are measured by the Δ parameter. The results for Δ are summarized in columns 4 and 5 of Table 2. The standard deviations are, for the most part, substantially larger than for T . Differences in the means between the O and S tubes are present at the 3σ level in Models 3 and 5, and at the 2σ level in models 2 and 6. The S tubes and saucers in Model 4 also differ at the 2σ level. The differences are in the sense that O tubes tend toward higher Δ and the saucers toward lower Δ compared to S tubes.

Roughly half the total standard deviation in Δ arises from a systematic inward radial gradient in the start space, reflecting a greater average elongation of the velocity fields of thin tubes compared with fat tubes. This effect is illustrated in Figure 3, which shows the normalized velocity fields of the nearly planar orbits (2,.55,.02) and (2,.90,.02) along with their streamline fits. The confocal fit correctly reproduces the progressively greater elongation of the fat tube velocity field toward

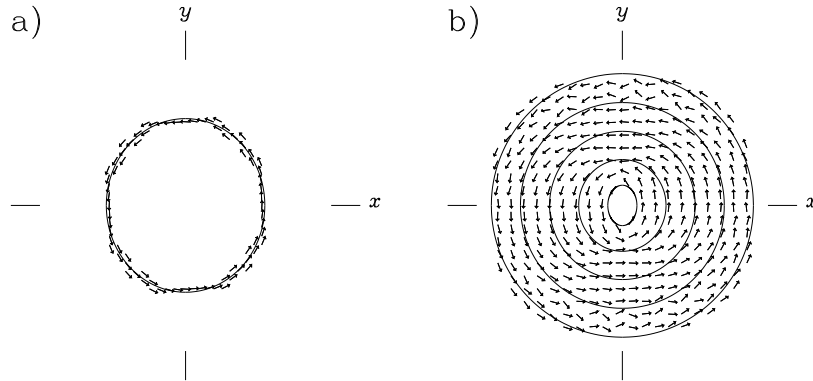


Fig. 3.— Normalized velocity fields of two nearly planar orbits: (a) (2,.55,.02); (b) (2,.90,.02). *Solid lines* show the streamline fits. Confocal streamlines correctly reproduce the greater elongation of the fat tube (b) toward smaller radii, but comparable elongations are reached at smaller radii compared to the thin tube.

smaller radius; but comparable elongations are reached at smaller radii compared to the thin tube. Since the fits average over volume this results in a smaller Δ for a fat tube than for a thin tube at the same energy. This means that adopting the elongation of thin tubes for all tubes would lead to an overestimate of the radial mean motions.

3.3. The O Tube/S Tube Boundary

The averages, $\langle T \rangle$ and $\langle \Delta \rangle$, over all orbits in a given model suggest an overall best-fit focal hyperbola with foci at $z = \pm \langle \Delta \rangle$, vertices at $z = \pm \langle \Delta \rangle (1 - \langle T \rangle)^{1/2}$, and asymptotes at $\sin^{-1} \langle T \rangle^{1/2}$ from the z axis. These hyperbolae are drawn as long-dashed curves in Figure 2. The agreement between the fitted hyperbolae and the actual O tube/S tube boundaries is remarkable. Remember that the fits are obtained solely from the mean velocity fields of the orbits, entirely without regard to the orbital *frequencies* which actually determine where the boundaries lie. Given the small variances in T and Δ , even a small number of orbits quite far from the boundary would suffice for a very good estimate.

The location of the O tube/S tube boundary is a direct measure of the triaxiality of the potential. That this quantity can be so accurately recovered from the (albeit 3-dimensional) mean orbital velocities compellingly supports the notion that triaxialities of real systems can be measured from their projected mean velocity fields.

3.4. Goodness of Fit

Figure 4 shows values of $\sin^{-1} Q$ (in degrees) plotted in the start spaces; this quantity is essentially the RMS angle between the velocity field and the fitted streamlines. It is under 10° for just under two thirds of the computed orbits, and under 23° for 90%. The larger values of $\sin^{-1} Q$ tend to occur close to the O/S boundary and among the fatter tubes, but also occasionally stand out as isolated poor fits in otherwise well-behaved regions.

The tendency for poorer fits among the fatter tubes is attributable to the radial gradient in the velocity field elongation shown in Figure 3b, but the situation near the O/S boundary is more complicated. In this region the time scale for an even wrapping of the invariant tori increases, and there is an abundance of high order resonant islands. Typically the result is a sort of “braided” velocity field, as one can see in Figure 1b and in the top and bottom of Figure 3b. For orbits trapped by a resonance this effect will not disappear when the orbit is run for a longer time or averaged with its reflections. However, this small scale structure is not a serious problem since it is unlikely to be resolved in any realistic observation, and can be seen to average out and match the streamlines in a coarser gridding of the velocity field.

We can identify nearly all of the isolated poor fits with specific high order resonances or slowly-diffusing regions of the stochastic web. These orbits are indicated by italics in Figures 2 and 4. Some resonances of comparatively low order produce substantial radial mean motions which do not cancel out when reflections are averaged, because the reflections do not visit the same regions of space. This effect is not very severe for the 1:1:2 resonance around which the saucer orbits lie, but does account for the consistently poorer fits compared to the surrounding S tubes. In general, the higher order the resonance, the better the fit, owing to the finer scale of velocity field braiding; good examples are orbits (2, .59, .39) and (2, .57, .45), apparently associated with 19:19:22 and 85:85:97 resonances, respectively. Finally, orbit (4, .36, .60) is genuinely stochastic and has a nearly random velocity field with a very weak residual net circulation about the x axis for the long integration performed.

4. Discussion

We have tested the viability of the *ansatz* of confocal streamlines for the mean stellar motions in elliptical galaxies by fitting such streamlines to velocity fields of individual orbits integrated in six scale-free potentials. We find that the great majority of orbits in each potential can be fitted by confocal systems with nearly the same T parameter and a fairly narrow range of Δ parameters. While there are statistically significant differences between the average T and Δ values obtained for O tubes, S tubes, and saucers, the differences are small enough that they can almost certainly be neglected in more complete models of galactic velocity fields. The accuracy with which the mean T and Δ for the computed orbits in a given potential recover the location of the O tube/S tube boundary is impressive, and supports the use of reasonably simple dynamical models to obtain

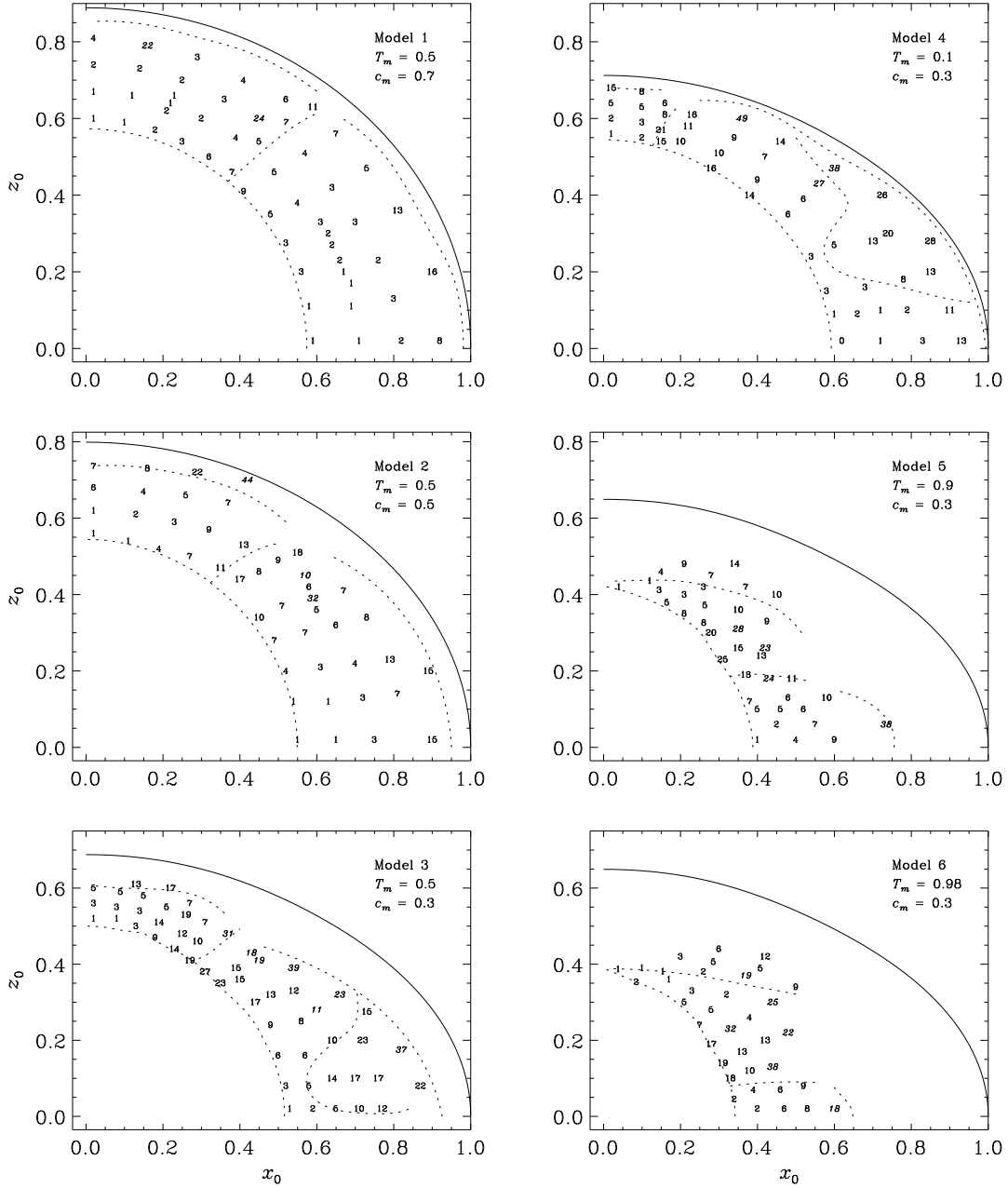


Fig. 4.— Start spaces as in Figure 2, showing the goodness of fit parameter $\sin^{-1} Q$ in degrees (cf. equation [4]); this is essentially the RMS angle between the velocity field and the fitted streamlines (section 3.4).

accurate statistical measurements of triaxiality from kinematic observations. Forthcoming papers will report on shape measurements using streamline-based velocity field models for NGC 1700, NGC 3379, NGC 4472, and the Davies and Birkinshaw (1988) sample of radio ellipticals. Such measurements may ultimately lead, for instance, to an understanding of the role of projection effects in determining the width of the fundamental plane, as well as to insights into the range of mechanisms responsible for elliptical galaxy formation.

It is, of course, a vast oversimplification to expect a single confocal system to *globally* fit any non-Stäckel potential. In this study we have considered only orbits at zero energy. In scale-free potentials the orbital structure is self-similar: each orbit at $E = 0$ can be scaled to a copy of itself at energy E according to $(x_0, z_0) \rightarrow (e^E x_0, e^E z_0)$. For this orbit our results would scale as $\Delta \rightarrow e^E \Delta$, $T \rightarrow T$, producing a set of similar streamlines. This is the “locally confocal” approximation used by Statler (1994a). Complications arise, however, when similar orbits overlap, since the elongations of the inner streamlines of the higher-energy copy will not match those of the outer streamlines of the lower-energy copy. In practice this will produce some intermediate elongation for the streamlines of the combined flow. Attempting to model this effect accurately would be impossible without making explicit assumptions for the form of the distribution function. A similar difficulty may be involved with the incompletely modeled radial motions of the saucer orbits, which are very sensitive both to the start space coordinates and the shape of the potential. But since it is dubious, at best, whether either of these effects could ever be discerned observationally, there is little benefit in overly-precise modeling.

A far more important effect that no one, including us, has yet dealt with properly is figure rotation. We have repeated a fraction of the orbit survey, rotating the potential about its short axis. At dimensionless pattern speeds Ω on the order of a few 10^{-2} or less we find that the S tube streamlines are mostly undisturbed, for both prograde and retrograde orbits. This would correspond to locations in the galaxy on the order of 1/10 of the corotation radius, or to figure rotation periods on the order of 10 dynamical times. The O tubes and box (as well as boxlet) orbits, however, are distorted in more complicated ways (de Zeeuw & Merritt 1983). Regular box orbits acquire a net prograde circulation in the rotating frame; we find a rather box-like mean flow around the perimeter of the orbit envelope. O tubes have their symmetry with respect to the yz plane broken, and averaged prograde-retrograde pairs show a complex circulation about the z axis. Neither of these effects can be approximated by confocal streamlines. More sophisticated methods will need to be developed to accurately model triaxial systems with rotating figures.

This work was supported by NASA Astrophysical Theory Program grants NAG5-2860 and NAG5-3050. We thank Suvendra Dutta for helpful comments on the manuscript.

REFERENCES

- Arnold, R., de Zeeuw, P. T., & Hunter, C. 1994, MNRAS, 271, 924
- Binney, J. 1985, MNRAS, 212, 767
- Binney, J. 1987, in Structure and Dynamics of Elliptical Galaxies, T. de Zeeuw, ed., (Dordrecht: Reidel), p. 229
- Binney, J. & Tremaine, S. 1987, Galactic Dynamics (Princeton: Princeton Univ. Press)
- de Zeeuw, T. & Merritt, D. 1983, ApJ, 267, 571
- de Zeeuw, T. 1985, MNRAS, 216, 273
- Franx, M., Illingworth, G. & de Zeeuw, T. 1991, ApJ, 383, 112
- Lauer, T. R., Ajhar, E. A., Byun, Y.-I., Dressler, A., Faber, S. M., Grillmair, C., Kormendy, J., Richstone, D., & Tremaine, S. 1995, AJ, 110, 2622
- Lees, J. & Schwarzschild, M. 1992, ApJ, 384, 491
- Lynden-Bell, D. 1962, MNRAS, 124, 95
- Merritt, D. & Fridman, T. 1996, ApJ, 460, 136
- Merritt, D. & Valluri, M. 1996, ApJ, 471, 82
- Miralda-Escudé, J. & Schwarzschild, M. 1989, ApJ, 339, 752
- Schwarzschild, M. 1993, ApJ, 409, 563
- Statler, T. 1991, AJ, 102, 882
- Statler, T. 1994a, ApJ, 425, 458
- Statler, T. 1994b, ApJ, 425, 500
- Statler, T. 1996, in Fresh Views of Elliptical Galaxies, A. Buzzoni, A. Renzini, & A. Serrano, eds. (San Francisco: Astronomical Society of the Pacific), p. 27
- Tenjes, P., Busarello, G., & Longo, G. 1992, Triaxial Elliptical Galaxies With Dust Lanes: An Atlas of Velocity Fields, (Napoli: Liguori editore).
- Tenjes, P., Busarello, G., Longo, G., & Zaggia S. 1993, A&A, 275, 61

Table 1. Model Shape Parameters

Model	Density		Potential		Streamlines
	T_m	c_m	T_p	c_p	$\langle T_{\text{fit}} \rangle$
1	0.50	0.7	0.472	0.889	0.480
2	0.50	0.5	0.467	0.799	0.473
3	0.50	0.3	0.479	0.688	0.508
4	0.10	0.3	0.096	0.712	0.111
5	0.90	0.3	0.883	0.649	0.898
6	0.98	0.3	0.976	0.630	0.969

Table 2. Averaged Streamline Parameters

Orbits	$\langle T \rangle$	σ_T	$\langle \Delta \rangle$	σ_Δ	N
Model 1: O	0.484	0.010	0.223	0.067	26
S	0.476	0.010	0.208	0.073	27
all	0.480	0.011	0.215	0.071	53
Model 2: O	0.477	0.011	0.315	0.057	16
S	0.464	0.026	0.280	0.070	28
all	0.473	0.032	0.297	0.081	46
Model 3: O	0.523	0.034	0.415	0.035	20
S	0.499	0.079	0.371	0.058	20
s	0.497	0.058	0.344	0.066	11
all	0.508	0.060	0.381	0.058	53
Model 4: O	0.112	0.009	0.337	0.046	10
S	0.097	0.041	0.346	0.102	28
s	0.163	0.037	0.297	0.044	8
all	0.111	0.043	0.335	0.087	46
Model 5: O	0.906	0.018	0.507	0.075	17
I	0.908	0.007	0.483	0.034	6
S	0.877	0.004	0.380	0.032	14
all	0.898	0.024	0.459	0.084	38
Model 6: O	0.970	0.021	0.434	0.153	20
I	0.970	0.019	0.425	0.126	9
S	0.965	0.004	0.356	0.044	8
all	0.969	0.018	0.415	0.134	37